Available online at www.sciencedirect.com

ScienceDirect

Green Energy & Environment 1 (2016) 91–99

www.keaipublishing.com/gee

Research paper

In-situ synthesis of interconnected SWCNT/OMC framework on silicon nanoparticles for high performance lithium-ion batteries

Weiwei Li [a,b], Shimou Chen [b], Jia Yu [b], Daliang Fang [b], Baozeng Ren [a,*], Suojiang Zhang [b,**]

[a] School of Chemical Engineering and Energy, Zhengzhou University, Zhengzhou 450001, China

[b] Beijing Key Laboratory of Ionic Liquids Clean Process, Key Laboratory of Green Process and Engineering, State Key Laboratory of Multiphase Complex Systems, Institute of Process Engineering, Chinese Academy of Sciences, Beijing 100190, China

Received 24 February 2016; revised 11 March 2016; accepted 14 March 2016
Available online 12 April 2016

Abstract

In spite of silicon has a superior theoretical capacity, the large volume expansion of Si anodes during Li^+ insertion/extraction is the bottle neck that results in fast capacity fading and poor cycling performance. In this paper, we report a silicon, single-walled carbon nanotube, and ordered mesoporous carbon nanocomposite synthesized by an evaporation-induced self-assembly process, in which silicon nanoparticles and single-walled carbon nanotubes were added into the phenolic resol with F-127 for co-condensation. The ordered mesoporous carbon matrix and single-walled carbon nanotubes network could effectively accommodate the volume change of silicon nanoparticles, and the ordered mesoporous structure could also provide efficient channels for the fast transport of Li-ions. As a consequence, this hybrid material exhibits a reversible capacity of 861 mAh g^{-1} after 150 cycles at a current density of 400 mA g^{-1}. It achieves significant improvement in the electrochemical performance when compared with the raw materials and Si nanoparticle anodes.

Keywords: Silicon; Single-walled carbon nanotube; Ordered mesoporous carbon; Lithium ion battery

1. Introduction

Lithium ion batteries (LIBs) are urgently needed as power supply for today's hybrid vehicles, portable electronic and medical devices owing to its high energy density and rechargeable properties [1]. With the increasing demand of LIBs with higher energy density and prolonged lifecycle, various cathode and anode materials with higher storage capacity have been investigated during the latest years [2,3]. On the one hand, the commercially used graphite carbon anode has a limited theoretical capacity of 372 mAh g^{-1}, which restricts its further application. Silicon has a theoretical capacity of 4200 mAh g^{-1} and a relatively low working potential, making it one of the most promising candidates for the next generation LIBs [4,5]. But silicon has the problem of huge volume expansion (>300%) during lithium insertion and extraction processes. Along with the pulverization and the exposure of more silicon fragments that consume more electrolyte, the impairment of the electrical contact between the current collector and active materials and continuous formation of solid–electrolyte interface (SEI) layers result in intensified capacity fading with prolonged cycles.

In order to overcome these difficulties, numerous efforts have been tried to reduce the volume expansion of silicon anodes. One strategy is decreasing the silicon particle size to micro or nanometre scale [6], such as silicon nanowires [7–9], double-walled silicon nanotubes [6,10], silicon nanoparticles [11–15], and silicon nanospheres [16,17]. Owing to the small particle size and available void space, the abnormal pressure generated during lithiation/delithiation process in these silicon nanostructures can be buffered effectively. Another way is

* Corresponding author.
** Corresponding author.
E-mail addresses: renbz@zzu.edu.cn (B. Ren), sjzhang@home.ipe.ac.cn (S. Zhang).

http://dx.doi.org/10.1016/j.gee.2016.04.005

dispersing silicon nanoparticles into a matrix [6,18], which possesses high conductivity and good mechanical properties, such as silicon/single-walled carbon nanotube (SWCNT) composite paper [19], graphene-encapsulated silicon foam [20], graphene nanosheets [21,22], carbon nanotubes [6,23−26] and hollow or porous carbon [18,27]. These silicon/carbon composites can not only improve the electric conductivity of the Si, but also accommodate the volume expansion of Si anodes and facilitate the formation of a stable SEI layer.

Among all the carbon materials, the ordered mesoporous carbon (OMC) with porous structure and large surface area can increase the contact area between active materials and the electrolyte, while facilitating the lithium ion diffusion in the electrolyte. So the OMC can be expected to improve the rate capability of Si-based anodes owing to its high specific surface area, ordered mesoporous channels and high pore volume. The silicon nanoparticles trapped in the OMC can also achieve a good rate capability [28−31]. However, the OMC exhibits a rather poor electric conductivity [32,33], which is different from other carbon materials (eg, carbon nanotube, graphene), resulting in that the OMC cannot solely be used as a matrix or additive to make up for the poor electric conductivity of the silicon anode. Considering the SWCNTs, which have high electric conductivity and flexible properties. It is suitable for constructing network to accommodate the expansion of Si-based anodes, as well as increasing the electric conductivity of Si and OMC. Herein, we have fabricated a ternary Si/SWCNT/OMC nanocomposite through a self-assembly synthesis process, in which the OMC was prepared as previously reported [34]. The key synthesis procedure was mixing the Si nanoparticles and SWCNTs together in the F127/phenolic resol solution using the solvent evaporation-induced self-assembly method, thus the interconnected SWCNT/OMC framework was in-situ synthesized on silicon nanoparticles.

For this ternary Si/SWCNT/OMC hybrid material, the Si nanoparticles are well distributed into the interconnected SWCNT/OMC framework, through hydrogen bonds formed between large number of hydroxyl groups on the surface of Si nanoparticles and the F127/phenolic resol [34,35], possessing a number of advantages: 1) The Si nanoparticles are trapped inside the OMC framework and are not in direct contact with the electrolyte solution, the SEI films can be regarded as forming on the surface of the outmost OMC only. 2) The abundant ordered mesopores in the OMC can provide enough void space to accommodate the volume change of Si in the charging/discharging processes. 3) The SWCNTs possess unique 1-D tubular structure, excellent mechanical properties, and high electric conductivity. Meanwhile, its flexible properties could alleviate the volume expansion of Si, thus making sure of an improved cycling performance.

2. Experimental

2.1. Experimental chemicals

Triblock copolymer Plurnoic F127 (Mw = 12,600, PEO_{106}-b-PPO_{70}-b-PEO_{106}) was purchased from Sigma-Aldrich. Silicon nanoparticles (~50 nm) were purchased from Alfa Aesar. Original SWCNTs were purchased from XF nano. Formalin solution (37 wt.%) was purchased from Aladdin Reagent Crop. Phenol. NaOH, HCl, and ethanol were purchased from Sinopharm Chemical Reagent Crop.

2.2. Synthesis of ternary Si/SWCNT/OMC nanocomposite

The Si/SWCNT/OMC composite was prepared by the solvent evaporation-induced self-assembly process. The fabrication process consisted of four steps, preparation of F127/phenolic resol precursor solution, dispersion of silicon nanoparticles and SWCNTs in the F127/phenolic resol solution, thermopolymerization and calcination.

2.2.1. Preparation of F127/phenolic resol

The phenolic resol precursor was prepared by polymerizing phenol and formaldehyde (37 wt.%, 2.1 ml) under alkaline conditions [22]. The phenol (0.61 g, 6.48 mmol) was melted at 42 °C in NaOH aqueous solution (0.1 M, 15 ml) under stirring in a 250 ml flask, followed by the addition of 2.1 ml formaldehyde (37 wt.%). This was followed by violently stirring of the mixture for 1 h at 70 °C. Subsequently, the mixture was cooled to room temperature, and the pH was adjusted to 7.0 using HCl (0.6 M). During this whole process, a colour transition was observed, and the aqueous solution changed its colour from transparent to crimson and finally to yellow. The prepared mixture was dried under vacuum evaporation at 45 °C. The yellow polymeric liquid was dissolved in ethanol, centrifuged, and filtered to remove the precipitated NaCl. At the end, the polymeric liquid was dissolved in an appropriate amount of ethanol prior to be used. The F127 (1.0 g) was dissolved in 10.0 g of ethanol and stirred at 40 °C to form a clear solution. The precursor solution was mixed with the solution of F127, stirring for 10 min to get the F127/phenolic resol.

2.2.2. Preparation of acid-functionalized SWCNTs

The original SWCNTs had an average diameter of 1−2 nm and an average length of 5−30 μm. The SWCNTs were milled with in a mixture of concentrated HNO_3/H_2SO_4 (40 ml, 1:3/V:V), and sonicated for 3 h to prepare carboxylic acid-functionalized SWCNTs [36]. Finally, the suspension was filtered using deionized water until the pH reached 7. The acid functionalized SWCNTS were dried at 100 °C for 12 h under vacuum.

2.2.3. Preparation of ternary Si/SWCNT/OMC hybrid composite

Silicon nanoparticles had an average particle size of less than 50 nm and a purity of more than 98%. Si NPs and SWCNTs were dispersed in ethanol by sonicating for 3 h. This was followed by the addition of SWCNTs and Si NPs solution into the F127/phenolic resol, with a continuous stirring for 8 h. After mixing up the solutions, the mixture was transferred into petri dishes, waiting for about 12 h until the ethanol was

evaporated at room temperature and the resol was transformed to a transparent membrane. It was then cured for thermopolymerization at 110 °C for more than 24 h. Finally, the membrane was carbonized at 350 °C for 5 h to remove the F127 template, and then heated from 350 °C to 600 °C for another 5 h under a stream of flowing argon gas at a heating ramp of 1 °C min^{-1} in a quartz tube furnace.

The ternary Si/SWCNT/OMC nanocomposite was prepared by adding different silicon content to the F127/phenolic resol, and the addition of the SWCNT was fixed at 10% against the total mass for all samples [33]. Depending on the silicon content, materials were labelled as Si-0.17/SWCNT/OMC, Si-0.41/SWCNT/OMC and Si-0.58/SWCNT/OMC. In a controlled experiment, the pure ordered mesoporous carbon without Si NPs and SWCNTs was made using the same method, named as OMC.

2.3. Material characterizations

The morphology and microstructure of the samples were characterized by field-emission scanning electron microscopy (SEM, Hitachai SU8020) and high-resolution transmission electron microscopy (HR-TEM, JEOL JEM-2100F). The wide-angle X-ray diffraction patterns were recorded on a X-ray diffractometer (XRD, Rigaku, Smartlab) with a Cu-$K_{\alpha 1}$ radiation source (9 kW, $\lambda = 0.15406$ nm). N_2 adsorption–desorption isotherms were measured using a volumetric adsorption analyzer (ASAP 2460, Micromeritics). The Brunauer–Emmett–Teller (BET) method was utilized to calculate the specific surface area. The pore volume and pore size distributions were calculated on the basis of the adsorption branches of the isotherms using the Barrett–Joyner–Halenda (BJH) method. The Raman spectra were recorded on a (LabRAM HR800, Horiba Jobin-Yvon) using Ar-ion laser of 514 nm. The mass percentage of silicon in the Si/SWCNT/OMC materials was obtained by thermogravimetric analysis (TGA), the TGA was carried out on a (STA7200RV, Hitachi High-Tech) apparatus from 25 °C to 800 °C under air atmosphere at a heating rate of 10 °C min^{-1}.

2.4. Electrochemical measurements

Electrochemical measurements were carried out using coin-type half cells (2025 type) prepared in a glove box filled with high purity argon. The cell contained the as-prepared electrode, using the pure lithium as the counter electrode and a Celgard 2025 polyethylene film as the separator, and the electrolyte solution of 1 M $LiPF_6$ in a 1:1:1 (w/w/w) mixture of ethylene carbonate, dimethyl carbonate and ethyl methyl carbonate. The anode electrode was composed of Si/SWCNT/OMC composite (80 wt.%), polyvinylidene fluoride binder (10 wt.%), and Super P carbon black (10 wt.%), which was uniformly cast onto the copper foil and dried under vacuum. Galvanostatic charge/discharge experiments were tested on a LAND battery testing system in the voltage range of 0.0–2.8 V at room temperature. Cyclic voltammetry (CV) data were recorded on a CHI660E electrochemical workstation at a scanning rate of 0.1 mV s^{-1}. Electrochemical impedance spectroscopy (EIS) measurement tests were carried out on an ACM Gill-AC-4 electrochemical station between 100 kHz and 0.1 Hz and the amplitude was 5 mV.

3. Results and discussion

A schematic illustration of the fabrication of the ternary Si/SWCNT/OMC nanocomposite is given in Fig. 1. The phenolic resol acted as the carbon source and the Pluronic F127 as a structure-directing agent as well as a sacrificial template for the formation of the ordered pore canal in the OMC. The phenol resol had a large number of hydroxyl groups, which

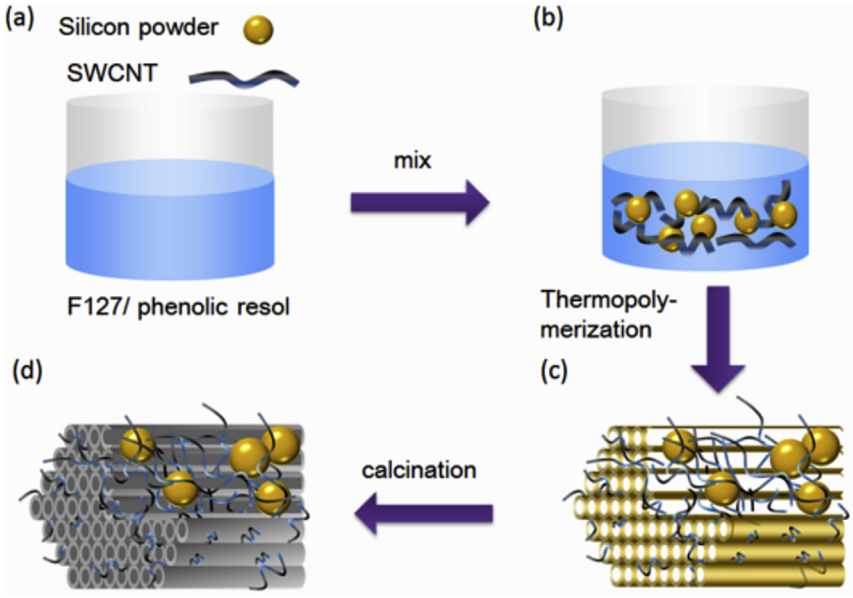

Fig. 1. Schematic illustration of the synthesis for the Si/SWCNT/OMC nanocomposite.

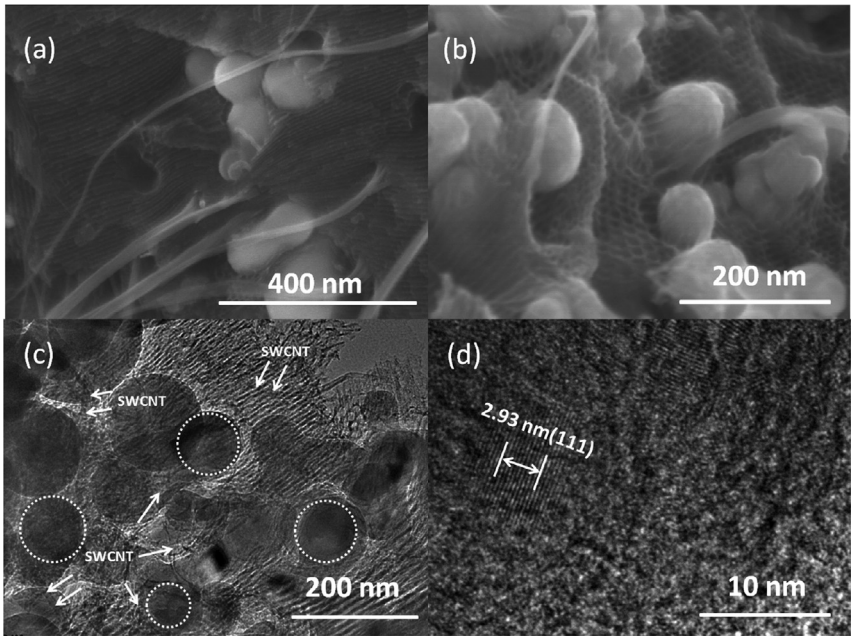

Fig. 2. (a) The SEM, (b) HRSEM and (c) TEM of the ternary Si/SWCNT/OMC nanocomposite with 41 wt.% of Si. (d) Corresponding HRTEM image showed the highly crystalline nature of the Si nanosphere and a preferential (111) orientation.

could interact with numerous polyether segments and terminal hydroxyl groups of the Pluronic F127 or the oxygen-containing functional groups on the surface of the Si NPs and SWCNTs to form weak covalent bonds or physical adsorption [37]. In order to make sure that the silicon nanoparticles were uniformly distributed in the matrix, the Si/ethanol solution was added to the above mixture drop by drop. The mixture was aged along with the gradual evaporation of ethanol. At the same time, the mesostructured polymer resols were formed, and transformed to an ordered liquid transparent mesophase. This could make the Si NPs distributed and trapped in the mixture uniformly and tightly. During the thermopolymerization process, the phenolic resin phase was carbonized to form interconnected SWCNT/OMC framework. After the calcination, F127 was decomposed to create the mesopores (Fig. S1, Supporting Information). Thus, the interconnected SWCNT/OMC framework was in-situ synthesized on the silicon nanoparticles.

Fig. 2a and b show the SEM images of the surface of the ternary Si/SWCNT/OMC nanocomposite that consists of Si NPs, SWCNTs and OMC. Due to the difference in structure of the three materials, there are ripples and wrinkles formed in the OMC. Besides, the SEM images show the inside structure of the nanocomposite, in which Si NPs are observed as white spheres dispersing in the interconnected SWCNT/OMC framework uniformly. Moreover, Si NPs are embraced by the interconnected SWCNT/OMC framework, and a thin layer of OMC is coated on the surface of the silicon nanoparticles (Fig. S1, Supporting Information). Furthermore, a much clearer structure can be seen in the Fig. 2c. The Si NPs marked in white circles and the ordered mesopores of the OMC are observed unambiguously, and the SWCNT marked in white arrows can be only observed at the edge of the material as a result of the OMC covering them inside. It can be presumed that Si NPs were welded into the SWCNT/OMC network instead of being simply physically immobilized. The OMC can act as a "binder" to weld Si nanoparticles and SWCNTs into the OMC framework to increase the mechanical stability of the electrode. In Fig. 2d, the lattice fringes of the (111) plane, corresponding to a d spacing of 2.93 Å, are observed for the Si NPs surrounded by the SWCNT/OMC framework. The SEM at low magnification of the surface of the ternary material can be seen in Fig. S1, Supporting Information. The wormhole mesopores in the SWCNT/OMC framework can not only provide efficient transport pathway for the lithium ions, but also offer void space to accommodate the volume change of the Si NPs, maintaining excellent cycling performance for LIB applications [38]. On the other hand, the addition of SWCNTs can improve the electric conductivity of the whole composite and keep the OMC from collapsing during the carbonization process.

The mesoporous structure in the OMC and ternary Si/SWCNT/OMC nanocomposite with different silicon content of 17 wt.%, 41 wt.% and 58 wt.% was investigated by the nitrogen adsorption/desorption isotherms (Fig. 3a) and Barrettt–Joyner–Halenda (BJH) pore size distributions (Fig. 3b). The four Nitrogen sorption isotherms in Fig. 3a exhibit representative type IV isotherm curves. The curve of the OMC has a sharp condensation step at a relative pressure of 0.4–0.8, suggesting a narrow pore size distribution and a type H1 hysteresis loop for mesoporous structure. In addition, the curves of the Si-0.17/SWCNT/OMC, Si-0.41/SWCNT/OMC and Si-0.58/SWCNT/OMC all reveal a type H1 hysteresis loop, indicating a well-maintained mesoporous structure in the

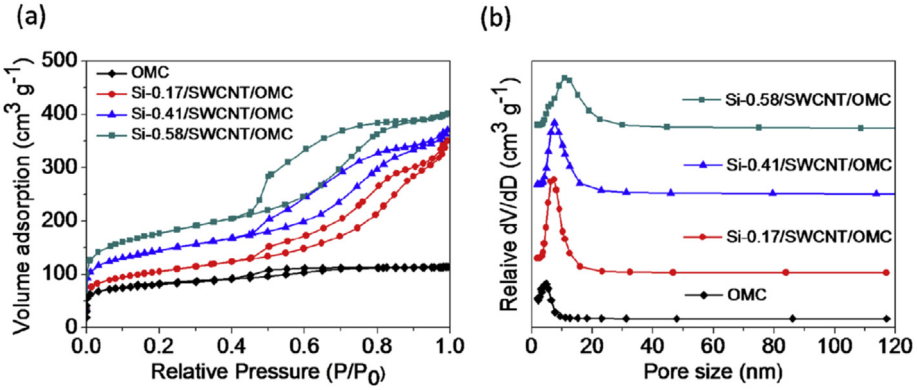

Fig. 3. (a) N_2 adsorption/desorption isotherms and (b) pore size distributions for OMC and Si/SWCNT/OMC nanocomposites with different silicon content of 17 wt.%, 41 wt.% and 58 wt.%.

final nanocomposites. Otherwise, there is a limiting adsorption at high P/P_0, which might be due to the addition of silicon nanoparticles and SWCNTs filling in the interparticle textural pores [28].

The maximum pore widths are shown in the Fig. 3b. The PSD curves increase from 3.6 to 8.6 nm with the enhancing of Si NPs amount, indicating that the mesoporous channels of the OMC are retained and unblocked. Moreover, the decrease of the surface area with the increase of Si NPs is ascribed to the addition of Si NPs and SWCNTs [39,40]. The data of surface area, pore volume and pore size are showed in Table S1, Supporting Information. Due to the composite was synthesized as a mesoporous material, the specific surface area was greatly influenced by the calcination temperature. In terms of the as-prepared OMC, when the calcination temperature was 600 °C, the BET surface area of OMC was 599 $m^2 g^{-1}$. At 900 °C, the BET surface area could reach up to 818 $m^2 g^{-1}$. However, the higher specific surface area is not good for the anode of LIBs, due to the more electrolyte may be consumed, leading to a reduced lifecycle [41]. So the calcination temperature was designed as 600 °C. The BET surface area of the Si-0.17/SWCNT/OMC, Si-0.41/SWCNT/OMC and Si-0.58/SWCNT/OMC is 602 $m^2 g^{-1}$, 488 $m^2 g^{-1}$ and 361 $m^2 g^{-1}$, respectively. In summary, the BET surface area decreases with the addition of the silicon component, but the average pore size is just the opposite.

The existing carbon species was demonstrated by Raman spectroscopy. The corresponding Raman spectra of Si-0.41/SWCNT/OMC nanocomposite are shown in the Fig. 4a, together with the pristine material OMC and SWCNTs spectra as a contrast. The peak locating at 520 cm^{-1} in the bottom line, is related to the crystalline silicon Raman phonon vibration, which confirms the presence of the crystallized Si in the Si-0.41/SWCNT/OMC sample. Besides that, other peaks in the Si-0.41/SWCNT/OMC sample match well with the pristine material OMC and SWCNTs, indicating that the crystalline structure of OMC and SWCNTs is not affected by the synthesis process. Furthermore, carbon materials have two broad bands at around 1358 cm^{-1} and 1590 cm^{-1}. They represent a disorder band (D-band) and a strong graphitic band (G-band), which can be attributed to in-plane vibrations of disordered amorphous carbon and crystalline graphitic carbon, respectively. The graphitization degree of the carbon materials can be calculated by the ratio of the intensity of the D band to the G band (I_D/I_G). From the Raman spectra, the calculated I_D/I_G of SWCNTs, OMC and Si-0.41/SWCNT/OMC is 0.29, 0.65 and 0.85, respectively, indicating that the graphitization degree of the hybrid materials decreases, when compared to the

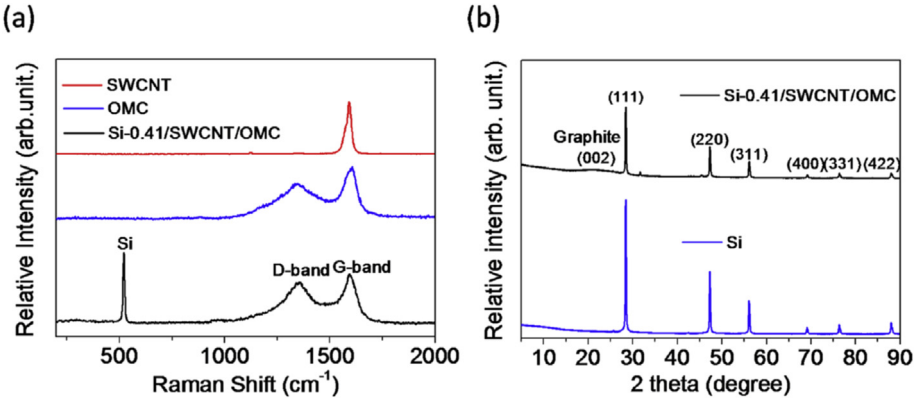

Fig. 4. (a) Raman spectra of the OMC, SWCNTs and the synthesized Si-0.41/SWCNT/OMC sample. (b) Wide-angle XRD patterns for Si and the synthesized Si-0.41/SWCNT/OMC sample.

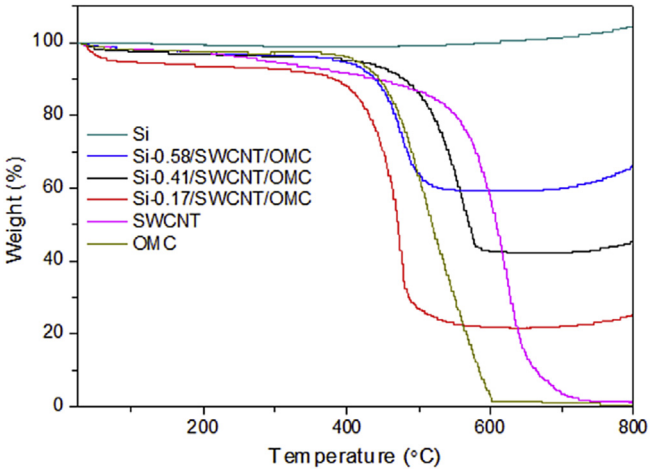

Fig. 5. TGA curves of OMC, SWCNTs, Si and the synthesized Si/SWCNT/OMC materials at a heating rate of 10 °C min^{-1} in air.

pristine OMC and SWCNTs. Fig. 4b shows the XRD patterns of Si-0.41/SWCNT/OMC nanocomposite, and pure silicon nanoparticles for comparison. The XRD pattern of the Si-0.41/SWCNT/OMC nanocomposite shows six well-resolved diffraction peaks, which match well with those of the pristine silicon nanoparticles. In addition, its other peaks also match well with the OMC and SWCNTs (Fig. S2, Supporting Information). The results indicate that the addition of SWCNTs and OMC has no effect on the crystal structure of silicon nanoparticles.

Furthermore, the silicon content in the synthesized Si/SWCNT/OMC nanocomposite was estimated by the thermogravimetric analysis (TGA), and the results are shown in Fig. 5. When the temperature increases to 450 °C, the OMC and the SWCNTs start decomposition, and completely disappear at about 600 °C and 700 °C, respectively. At 700 °C, the mass increase of the Si/SWCNT/OMC nanocomposite can be attributed to the oxidization of the silicon. According to the TGA results, the content of silicon in the three Si/SWCNT/OMC hybrid materials is estimated to be 17 wt.%, 41 wt.% and 58 wt.%, respectively. The mass percentage of SWCNTs to the total weight is fixed at 10 wt.% for all the Si/SWCNT/OMC nanocomposite as designed in advance (see for details in the experimental section).

The electrochemical performance of the Si/SWCNT/OMC nanocomposite was investigated through galvanostatic charge/discharge cycles. For comparison, the electrochemical performance of the pure OMC, pure SWCNT and pure Si NPs

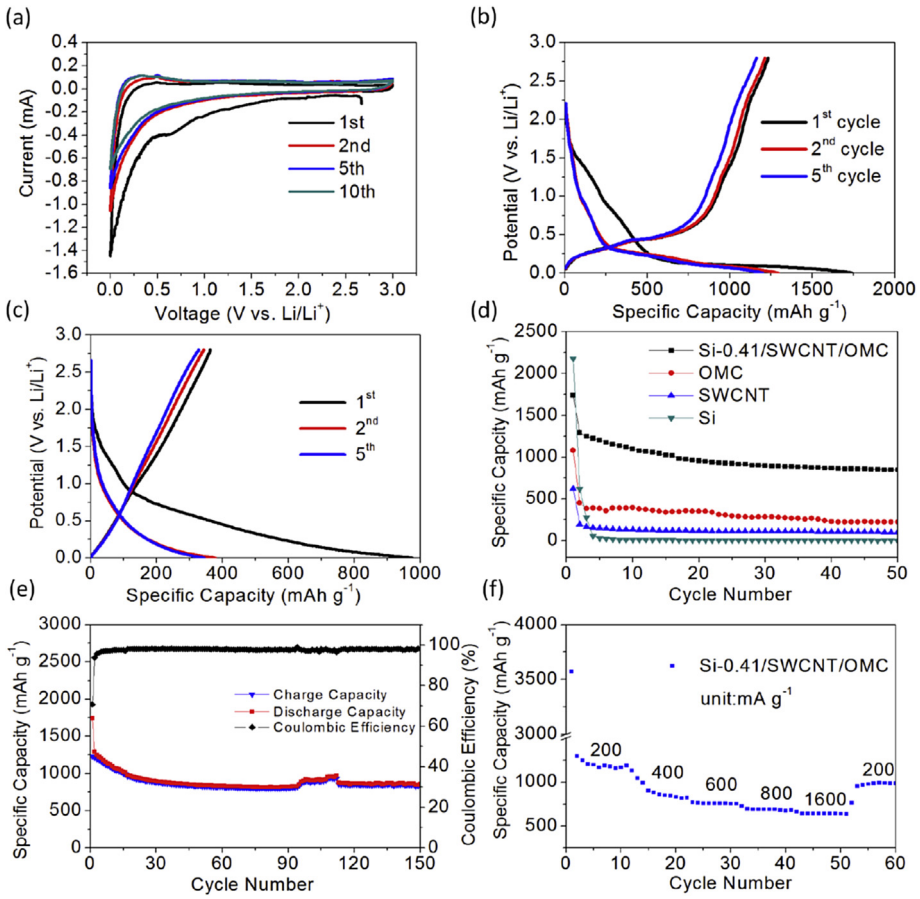

Fig. 6. (a) CV curves of Si-0.41/SWCNT/OMC nanocomposite for the 1st, 2nd, 5th and 10th cycles at a scan rate of 0.1 mV s^{-1} between 0.0 and 3.0 V. (b) The 1st, 2nd, and 5th charge/discharge profiles of Si-0.41/SWCNT/OMC at 400 mA g^{-1} as a LIB anode. (c) The 1st, 2nd, and 5th charge/discharge profiles of OMC at a current density of 400 mA g^{-1} as a LIB anode. (d) Comparison of the cycling performance of the Si-0.41/SWCNT/OMC, pure OMC, pure SWCNT and pure Si at a current density of 400 mA g^{-1}. (e) Cycling performance and coulombic efficiency of the Si-0.41/SWCNT/OMC at a current density of 400 mA g^{-1}. (f) Rate capabilities from 200 mA g^{-1} to 1600 mA g^{-1} of Si-0.41/SWCNT/OMC.

was also tested as control groups under the same conditions. Fig. 6a shows the CV curves of Si-0.41/SWCNT/OMC composite for the 1st, 2nd, 5th and 10th cycles at a scan rate of 0.1 mV s^{-1} within a potential window of 0.0–3.0 V. It is clear that the first cycle is different from the subsequent cycles. The first cycle discharge current become quite large below 0.1 V, which is due to the reaction between crystalline silicon and lithium that generates amorphous Li_xSi [42]. A broad cathodic peak appears around 0.6 V in the first discharge curve and disappears in the subsequent cycles, which can be related to the formation of SEI layers on silicon, as well as the side reaction of lithium ions with the OMC. The redox peak at 0.3 V and 0.5 V in the anodic branch can be observed from the second cycles, which corresponds to delithiation of amorphous (α) α-Li_xSi converted to α-Si. In addition, the increasing intensity of the two current peaks in the subsequent cycles is related to the gradually electrochemical activation of the electrode [43].

Fig. 6b and c show the galvanostatic charge/discharge curves of the Si-0.41/SWCNT/OMC nanocomposite and OMC electrodes at a current density of 400 mA g^{-1} within the voltage window of 0.01–2.8 V vs Li^+/Li for the 1st, 2nd and 5th cycles. Their specific capacities were calculated against the total mass of Si/SWCNT/OMC composite and OMC material, respectively. As shown in Fig. 6b, in the first discharge profile, the potential decreases quickly with the reduction of Li content and is followed by a long flat plat at about 0.1 V, which is a typical lithiation behaviour character of crystal Si anodes, corresponding to the lithium potential of pure crystalline silicon [6,37,44,45]. The sharp decrease of potential in the high potential area may be mainly ascribed to the lithiation of the OMC (Fig. 6c). The initial discharge capacity of Si-0.41/SWCNT/OMC anode is 1741 mAh g^{-1} with a reversible charge capacity of 1233 mAh g^{-1}, showing an initial coulombic efficiency of 70.8%. The relatively high irreversible capacity is mainly ascribed to the high specific surface area of the OMC, resulting in the more formation of SEI layers, which can be evidenced by the extremely low coulombic efficiency of 36% for the OMC anode (Fig. 6c).

To investigate the effect of Si content on electrochemical performance of the ternary Si/SWCNT/OMC nanocomposite, the cycling performance of Si-0.17/SWCNT/OMC, Si-0.41/SWCNT/OMC, and Si-0.58/SWCNT/OMC were investigated at the same condition (Fig. S3, Supporting Information). After 50 cycles, the Si-0.17/SWCNT/OMC and Si-0.58/SWCNT/OMC anodes deliver discharge specific capacities of 393 mAh g^{-1} and 750 mAh g^{-1} respectively, which are lower than the capacity of 848 mAh g^{-1} for the Si-0.41/SWCNT/OMC anode. The result reveals that the Si content of 41 wt.% in the nanocomposite should be the best one for the cycling performance as anodes for LIBs.

Fig. 6d shows the discharge capacities vs cycle number profiles of the Si-0.41/SWCNT/OMC, OMC, SWCNTs and Si anodes. The irreversible capacity of the Si-0.41/SWCNT/OMC anode in the first cycle induced by SEI formation is similar to other anodes, but this anode exhibits more stable cycling properties in the following cycles. After 50 charge/discharge cycles, the Si-0.41/SWCNT/OMC composite delivers a reversible discharge capacity of 848 mAh g^{-1}, which is almost 4 times larger than that of the OMC anode (222 mAh g^{-1}). The role of OMC in the ternary anode is to provide a stable mechanical support and electrochemical network. It is suggested that the improvement of the ternary Si-0.41/SWCNT/OMC nanocomposite was ascribed to the uniform cylindrical pore structure of the mesopores of OMC, nanosized active silicon nanoparticles and the co-existence of high electric conductivity of SWCNTs. In order to see the buffer effect of the OMC on volume expansion of Si, the more cycling performance and corresponding coulombic efficiency of the Si-0.41/SWCNT/OMC anode are shown in Fig. 6e. It shows that the discharge specific capacity remains to be 861 mAh g^{-1} after 150 cycles. In Fig. 6f, the capacity gradually decreases with the current density increasing from 200 mA g^{-1} to 1600 mA g^{-1}, and a discharge specific capacity of nearly 640 mAh g^{-1} is still remained even at 1600 mA g^{-1}. When the current density recovers to 200 mA g^{-1}, it still displays a retention capacity of 989 mAh g^{-1}, showing a good rate capability. This performance is much better than other reported Si based anode materials [18,19,46–52]. These results prove that the OMC can restrain the stress of volume expansion and thus improves the electrochemical stability of the composite.

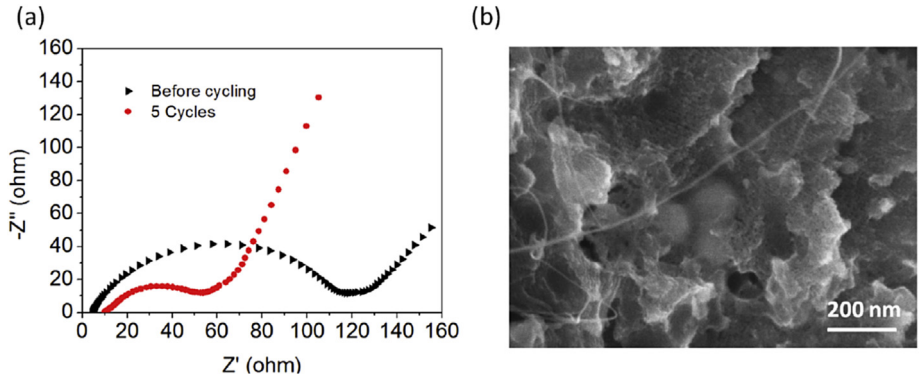

Fig. 7. (a) Nyquist plots of Si-0.41/SWCNT/OMC anode before cycling and after 5 cycles. (b) HR-SEM images of the Si-0.41/SWCNT/OMC anode after 50 cycles at a current density of 400 mA g^{-1}.

The electrochemical impedance spectroscopy of the ternary Si-0.41/SWCNT/OMC nanocomposite anode was investigated to further understand the mechanism for the improved cycling performance. Fig. 7a shows the Nyquist plots of the Si-0.41/SWCNT/OMC anodes before cycling and after 5 charge/discharge cycles, both of the curves consist of a depressed semicircle in the high-to-medium frequency regions and an oblique line in the low frequency region. The depressed semicircles at high frequencies are related to the resistance of SEI layers and charge transfer resistance, while the slopping lines in the low frequency region correspond to the lithium ion diffusion [53]. It is clear that, the electrodes show decreased values of charge transfer resistance in comparison with before cycling and after 5 cycles, which may be attributed to the activation of the electrodes and the sufficient contact between the electrolyte and activated materials. To investigate the structural stability during repeated cycling, the morphology of Si-0.41/SWCNT/OMC nanocomposite was observed after 50 fully lithiation/delithiation cycles at a current density of 400 mA g^{-1}. In Fig. 7b, the HR-SEM image shows that the silicon nanoparticles still have an unbroken structure, and its volume does not change exaggeratedly. In addition, the SWCNT/OMC framework still exhibits a stable 3D interconnected network, and SEI layers can only be formed on the outmost OMC cloth, which can prevent the silicon nanoparticles from contacting with the electrolyte directly, indicating a good cycling performance of this anode.

On the basis of above results, the excellent electrochemical performance of the Si/SWCNT/OMC electrode is due to the synergetic effect between SWCNTs and OMC. They form interconnected conductive framework, which can benefit the fast transport of both electrons and lithium ions, and thus improves the electrode kinetics. Firstly, the small particle size of Si NPs (~50 nm) are coated with OMC layers, which can restrain the volume expansion of silicon nanoparticles during Li^+ insertion/extraction and offer short distance for lithium and electron diffusion. The interconnected SWCNT/OMC framework can enhance the electrodes stability by welding silicon nanoparticles, to prevent their exfoliation from electrodes. It can serve as an effective matrix to prevent them from aggregating during electrochemical cycling. Secondly, the existence of SWCNT/OMC framework around the Si nanoparticles remarkably increases the electric conductivity of the nanocomposite, which leads to an improved high rate charge/discharge performance. Because the traditional graphite anode with turbostratic structures usually slow down the lithium diffusion rates within their frameworks, thus limiting the rate capabilities. The uniform mesopores in the OMC can reduce the solid-state diffusion pathway for Li ions and provide fast transport channels for lithium and electron diffusion. And the SWCNTs in the SWCNT/OMC framework can not only improve the electric conductivity of the OMC, but also can provide sufficient void space to relieve the huge volume expansion of silicon. Thirdly, silicon nanoparticles and SWCNTs are embedded in the OMC cloth. It permits a stable SEI to be formed of the OMC and prevent continual rupturing and reformation of the SEI, which can reduce the direct contact between the Si and the electrolyte. Moreover, the ordered mesopores in the OMC can not only provide sufficient space to accommodate the volume expansion of Si anodes, but also offer more contact area between active material and the electrolyte solution. It is very important for the stability and capacity retention of the Si during cycles.

4. Conclusions

In conclusion, Si/SWCNT/OMC nanocomposites used as an anode material have been synthesized by a solvent evaporation-induced self-assembly process. The SWCNT/OMC framework is in-suit synthesized on the surface of silicon nanoparticles. A thin layer of OMC is coated on the surface of well distributed silicon nanoparticles, preventing the silicon nanoparticles from contacting the electrolyte directly. Thus SEI layers can only be formed on the outmost OMC cloth. In addition, the SWCNT/OMC framework provides a rapid electron transport path, and better performance results from the synergistic effects between the SWCNT and OMC. When the hybrid materials are used as anodes for LIBs, the electrical performance can be controlled by optimizing the weight ratio of the silicon content. In a typical experiment, the Si-0.41/SWCNT/OMC sample displays a high discharge specific capacity of 861 mAh g^{-1} at a current density of 400 mA g^{-1} after 150 cycles. The performance of the synthesized material is much better than many Si based anodes reported. In addition, the whole preparation procedure is simple, controllable and low-cost, which could be easily scaled up for mass production. The good performance and the advantages of the preparation method make the Si/SWCNT/OMC composite a promising electrode material for the next-generation electrochemical energy storage devices.

Conflict of interest

The authors declare no conflict of interest.

Acknowledgements

This work was supported by the National Natural Science Foundation of China (NO. 91434203, 21276257, 91534109), “Strategic Priority Research Program” of the Chinese Academy of Sciences (Grant No. XDA09010103), and External Cooperation Program of BIC of the Chinese Academy of Sciences (Grant No. GJHZ201306).

Appendix A. Supplementary data

Supplementary data related to this article can be found at http://dx.doi.org/10.1016/j.gee.2016.04.005.

References

[1] J.B. Goodenough, Y. Kim, Chem. Mater. 22 (2010) 587–603.

[2] W.J. Hao, S.M. Chen, Y.J. Cai, L. Zhang, Z.X. Li, S.J. Zhang, J. Mater. Chem. A 2 (2014) 13801–13804.
[3] X.Y. Liu, S.M. Chen, J. Yu, W.L. Zhang, Y.J. Dai, S.J. Zhang, RSC Adv. 5 (2015) 7388–7394.
[4] H. Wu, Y. Cui, Nano Today 7 (2012) 414–429.
[5] C.K. Chan, H. Peng, G. Liu, K. McIlwrath, X.F. Zhang, R.A. Huggins, Y. Cui, Nat. Nanotechnol. 3 (2008) 31–35.
[6] M.H. Park, M.G. Kim, J. Joo, K. Kim, J. Kim, S. Ahn, Y. Cui, J. Cho, Nano Lett. 9 (2009) 3844–3847.
[7] L.F. Cui, R. Ruffo, C.K. Chan, H.L. Peng, Y. Cui, Nano Lett. 9 (2009) 491–495.
[8] Z.S. Wen, Z.Y. Zhang, G.Q. Wang, RSC Adv. 4 (2014) 57430–57435.
[9] Y.Q. Qu, H.L. Zhou, X.F. Duan, Nanoscale 3 (2011) 4060–4068.
[10] H. Wu, G. chan, J.W. Choi, I. Ryu, Y. Yao, M.T. McDowell, S.W. Lee, A. Jackson, Y. Yang, L. Hu, Y. Cui, Nat. Nanotechnol. 7 (2012) 310–315.
[11] B. Liu, P. Soares, C. Checkles, Y. Zhao, G. Yu, Nano Lett. 13 (2013) 3414–3419.
[12] C.L. Ma, C. Ma, J.Z. Wang, H.Q. Wang, J.L. Shi, Y. Song, Q.G. Guo, L. Liu, Carbon 72 (2014) 38–46.
[13] Z.L. Xu, B. Zhang, J.K. Kim, Nano Energy 6 (2014) 27–35.
[14] J. Niu, S. Zhang, Y. Niu, H.H. Song, X.H. Chen, J.S. Zhou, B. Cao, J. Mater. Chem. A 3 (2015) 19892–19900.
[15] R. Yi, J. Zai, F. Dai, M.L. Gordin, D.H. Wang, Nano Energy 6 (2014) 211–218.
[16] H. Ma, F. Cheng, J. Chen, J.Z. Zhao, C.S. Li, Z.L. Tao, J. Liang, Adv. Mater. 19 (2007) 4067–4070.
[17] S.H. Park, D.J. Ahn, Y.M. Choi, K.C. Roh, K.B. Kim, J. Mater. Chem. A 3 (2015) 20935–20943.
[18] M.S. Wang, W.L. Song, J. Wang, L.Z. Fan, Carbon 82 (2015) 337–345.
[19] S.L. Chou, Y. Zhao, J.Z. Wang, Z.X. Chen, H.K. Liu, S.X. Dou, J. Phys. Chem. C 114 (2010) 15862–15867.
[20] J. Ji, H.X. Ji, L.L. Zhang, X. Zhao, X. Bai, X.B. Zhang, R.S. Ruoff, Adv. Mater. 25 (2013) 4673–4677.
[21] H.W. Mi, Y.L. Li, P.Y. Zhu, X.Y. Chai, L.N. Sun, H.T. Zhuo, Q.L. Zhang, C.X. He, J.H. Liu, J. Mater. Chem. A 2 (2014) 11254–11260.
[22] J.K. Feng, Z. Zhang, L.J. Ci, W. Zhai, Q. Ai, S.L. Xiong, J. Power Sources 287 (2015) 177–183.
[23] L.B. Hu, H. Wu, Y.F. Gao, A.Y. Cao, H.B. Li, J. McDough, X. Xie, M. Zhou, Y. Cui, Adv. Energy Mater. 1 (2011) 523–527.
[24] B. Hertzberg, A. Alexeev, G. Yushin, J. Am. Chem. Soc. 132 (2010) 8548–8549.
[25] B. Wang, X.L. Li, X.F. Zhang, B. Luo, Y.B. Zhang, L.J. Zhi, Adv. Mater. 25 (2013) 3560–3565.
[26] B.W. Weng, H. Lin, X. Chen, J. Ren, Z. Zhang, L. Qiu, G. Guan, H. Peng, J. Mater. Chem. A 2 (2014) 9306–9312.
[27] N. Liu, H. Wu, M.T. McDowell, Y. Yao, C.M. Wang, Y. Cui, Nano Lett. 12 (2012) 3315–3321.
[28] J. Park, G.P. Kim, I. Nam, S. Park, J. Yi, Nanotechnology 24 (2013) 025602.
[29] Y.R. Liang, L.F. Cai, L.Y. Chen, X.D. Lin, R.W. Fu, M.Q. Zhang, D.C. Wu, Nanoscale 7 (2015) 3971–3975.
[30] J. Balach, T. Jaumann, M. Klose, S. Oswald, J. Eckert, L. Giebeler, Adv. Funct. Mater. 25 (2015) 5285–5291.
[31] K. Han, Z. Liu, J.M. Shen, Y.Y. Lin, F. Dai, H.Q. Ye, Adv. Funct. Mater. 25 (2015) 455–463.
[32] X.Q. Wang, J.S. Lee, C. Tsouris, D.W. DePaoli, S. Dai, J. Mater. Chem. 20 (2010) 4602–4608.
[33] B.K. Guo, X.Q. Wang, P.F. Fulvio, M.F. Chi, S.M. Mahurin, X.G. Sun, S. Dai, Adv. Mater. 23 (2011) 4661–4666.
[34] Y. Meng, D. Gu, F.Q. Zhang, Y.F. Shi, H.F. Yang, Z. Li, C.Z. Yu, B. Tu, D.Y. Zhao, Angew. Chem. 44 (2005) 7053–7059.
[35] C.D. Liang, S. Dai, J. Am. Chem. Soc. 128 (2006) 5316–5317.
[36] R. Mo, S.O. Tung, Z.Y. Lei, G.Y. Zhao, K. Sun, N.A. Kotov, ACS Nano 9 (2015) 5009–5019.
[37] H. Wu, G.H. Yu, L.J. Pan, N. Liu, M.T. McDowell, Z.N. Bao, Y. Cui, Nat. Commun. 4 (2013) 1943.
[38] A. Gohier, B. Laïk, K.H. Kim, J.L. Maurice, J.P. Pereira-Ramos, C.S. Cojocaru, P.T. Van, Adv. Mater. 24 (2012) 2592–2597.
[39] P.F. Fulvio, R.T. Mayes, X.Q. Wang, S.M. Mahurin, J.C. Bauer, V. Presser, J. McDonough, Y. Gogotsi, S. Dai, Adv. Funct. Mater. 21 (2011) 2208–2215.
[40] S.H. Ng, J.Z. Wang, D. Wexler, K. Konstantinov, Z.P. Guo, H.K. Liu, Angew. Chem. Int. Ed. 45 (2006) 6896–6899.
[41] Q. Li, L.W. Yin, J.Y. Ma, Z.Q. Li, Z.W. Zhang, A. Chen, C.X. Li, Energy 85 (2015) 159–166.
[42] M.K. Datta, P.N. Kumta, J. Power Sources 194 (2009) 1043–1052.
[43] M.Q. Li, M.Z. Qu, X.Y. He, Z.L. Yu, J. Power Sources 188 (2009) 546–551.
[44] M.T. McDowell, I. Ryu, S.W. Lee, C.M. Wang, W.D. Nix, Y. Cui, Adv. Mater. 24 (2012) 6034–6041.
[45] I. Kovalenko, B. Zdyrko, A. Magasinski, B. Hertzberg, Z. Milicev, R. Burtovyy, I. Luzinov, G. Yushin, Science 334 (2011) 75–79.
[46] L. Shi, W.K. Wang, A.B. Wang, K.G. Yuan, Y.S. Yang, J. Mater. Chem. A 2 (2014) 20213–20220.
[47] W.F. Ren, Z.L. Zhang, Y.H. Wang, Q.Q. Tan, Z.Y. Zhong, F.B. Su, J. Mater. Chem. A 3 (2015) 5859–5865.
[48] Y. Zhang, Y.Z. Jiang, Y.D. Li, B.B. Li, Z.H. Li, C.M. Niu, J. Power Sources 281 (2015) 425–431.
[49] H.R. Zhang, X.Y. Qin, J.X. Wu, Y.B. He, H.D. Du, B.H. Li, F.Y. Kang, J. Mater. Chem. A 3 (2015) 7112–7120.
[50] C. Kim, S. Choi, S. Yoo, D. Kwon, S. Ko, J. Kim, S.Y. Lee, I.D. Kim, S. Park, Nanoscale 7 (2015) 11286–11290.
[51] J.X. Wu, X.Y. Qin, C. Miao, Y.B. He, G.M. Liang, D. Zhou, M. Liu, C.P. Han, B.H. Li, F.Y. Kang, Carbon 98 (2016) 582–591.
[52] Y. Zhou, H.J. Guo, Y. Yang, Z.X. Wang, X.H. Li, R. Zhou, W.J. Peng, Mater. Lett. 168 (2016) 138–142.
[53] Y.H. Xu, Y.J. Zhu, C.S. Wang, J. Mater. Chem. A 2 (2014) 9751–9757.